Article

The Optimization of Process Parameters and Microstructural Characterization of Fiber Laser Welded Dissimilar HSLA and MART Steel Joints

Celalettin Yuce *, Mumin Tutar, Fatih Karpat and Nurettin Yavuz

Department of Mechanical Engineering, Uludag University, Bursa 16059, Turkey; mumintutar@uludag.edu.tr (M.T.); karpat@uludag.edu.tr (F.K.); nyavuz@uludag.edu.tr (N.Y.)
* Correspondence: cyuce@uludag.edu.tr; Tel.: +90-224-294-1919

Abstract: Nowadays, environmental impact, safety and fuel efficiency are fundamental issues for the automotive industry. These objectives are met by using a combination of different types of steels in the auto bodies. Therefore, it is important to have an understanding of how dissimilar materials behave when they are welded. This paper presents the process parameters' optimization procedure of fiber laser welded dissimilar high strength low alloy (HSLA) and martensitic steel (MART) steel using a Taguchi approach. The influence of laser power, welding speed and focal position on the mechanical and microstructural properties of the joints was determined. The optimum parameters for the maximum tensile load-minimum heat input were predicted, and the individual significance of parameters on the response was evaluated by ANOVA results. The optimum levels of the process parameters were defined. Furthermore, microstructural examination and microhardness measurements of the selected welds were conducted. The samples of the dissimilar joints showed a remarkable microstructural change from nearly fully martensitic in the weld bead to the unchanged microstructure in the base metals. The heat affected zone (HAZ) region of joints was divided into five subzones. The fusion zone resulted in an important hardness increase, but the formation of a soft zone in the HAZ region.

Keywords: laser welding; dissimilar weld; parameter optimization; microstructural examination

1. Introduction

The automotive sector is focused on developing and manufacturing fuel saving, higher safety vehicles with cost efficient methods. This will be achieved through proper design and using lighter and stronger materials on the auto body parts. Therefore the utilization of advanced high-strength steels (AHSS) is widespread. Due to the higher strength and good formability properties, AHSS can replace conventional thicker materials used in vehicle bodies without comprising crashworthiness. Dual phase (DP), complex phase (CP), martensitic steel (MART) and transformation-induced plasticity (TRIP) steels are the most common types of the AHSS [1]. Among these AHSS types, MART steel is one of the strongest cold-rolled AHSS on the market and has become the preferred material for automotive body applications, such as side impact beams, bumpers and structural components. Although using AHSS steels in the automobile structure is increasing, due to specific mechanical properties, high strength low alloy (HSLA) steel is still mainly used for structural parts, such as cross members, longitudinal beams, chassis components, etc. [2].

Welding is one of the most used and essential joining technique in the fabrication of the auto body and plays a significant role in assessing the final mechanical and metallurgical properties of the joined parts [3]. Due to much superiority over conventional welding methods, such as non-contact and single

side access welding, low process cost and suitability of automation, laser welding is becoming an attractive and economically advantageous joining technique in the automotive industry [4]. Joints of dissimilar steel combinations in auto body structures are widely utilized for several applications requiring a special combination of properties besides cost saving and weight reduction. However, due to different metallurgical, thermal and physical properties of the materials, dissimilar material welding is more challenging than similar materials welding. Due to low and concentrated heat input and high speed properties, laser welding has also advantages on joining dissimilar materials over other conventional methods [5]. Thus, reduced distortion and a narrower heat affected zone (HAZ) with limited microstructural changes can be obtained.

There are several studies in the literature concerning the laser welding of similar or dissimilar DP and HSLA steels. Saha et al. [2] examined the mechanical and microstructural properties of laser welded DP980 and HSLA steel sheets. They stated that the tensile strength of the dissimilar welds was lower than DP welds. Xu et al. [6] investigated microstructural and mechanical properties, and Parkes et al. [7] reported the fatigue properties of laser welded DP and HSLA joints with varying weld geometries. Parkes et al. [8] evaluated the tensile properties of laser welded HSLA and DP steels at cryogenic, room and elevated temperatures. They reported that with the temperature increase, the tensile properties were decreased. In addition, several research works investigated laser welding of higher degree DP steels and AHSS. Wang et al. [9,10] investigated the effect of energy input and softening mechanism on the laser butt welded DP1000 steel. They found that the weld bead width and softening zone width become narrowed at lower energy input levels. Additionally, the mechanical properties were increased. The study of Rossini et al. [11], concerned with laser welding of dissimilar AHSS types, has shown that a fully martensitic microstructure was present in the 22MnB5, DP and TRIP steels close to the fusion zone (FZ), while mainly tempered martensite and ferrite zones were close to the base metal.

Although there are many research works about laser welding of DP and HSLA steels, only limited work has been reported on the laser welding of MART steels. Nemecek et al. [12] compared the microstructural and mechanical properties of MART steel joints made by laser and metal active gas (MAG) welding. They stated that the strength of the laser welded joints was higher than arc welding, and the HAZ width and grain coarsening in the HAZ were minimal. Zhao et al. [13] investigated the effect of welding speed on weld bead geometry and the tensile properties of the laser welded MART steel. They observed that, due to the fast cooling rate, the FZ of the joints contained predominantly martensite. Furthermore, the tensile load gradually increased with decreasing welding speed.

Due to welding process parameters directly affecting the quality of the weld joints, it is necessary to work in the suitable range. However, defining the suitable parameters to obtain the required quality welded joints is a time-consuming process. Several optimization methods are utilized in order to solve this problem. The Taguchi method is one of the most common design of experiment (DOE) techniques that allows the analysis of experiments with the minimum number [14,15]. In the literature, several researchers have used DOE methods to optimize quality characteristics in laser welding parameters. Benyounis and Olabi [16] have presented a review of the application of optimization techniques in several welding processes. Anawa and Olabi [17] used the Taguchi method for the purpose of increasing the productivity and decreasing the operation cost of laser welding ferritic-austenitic steel sheets. Another study of the authors [18] analyzed the optimized shape of dissimilar laser welded joints and fusion zone area depending the process parameters. Sathiya et al. [19] carried out the Taguchi method and desirability analysis to relate the parameters to the weld bead dimension and the tensile strength of the joints with various shielding gasses. Fiber laser welding has demonstrated its capability of welding dissimilar steel joint with and without the help of a synergic power source like the arc [20]. Acherjee et al. [21] used Taguchi, response surface methodology (RSM) and desirability function analyses in laser transmission welding, and they investigated the optimal parameter combination for the joint quality.

In addition to these studies, several researchers used other DOE methods to investigate the effect of laser parameters on the mechanical properties and bead geometries of laser welded joints. Benyounis et al. [22] examined the influence of process parameters on the weld bead geometry. They stated that weld bead dimensions were affected by the level of heat input. Ruggiero et al. [23] and Olabi et al. [24] showed the effects of the process parameters on the weld geometry and operating cost for austenitic steel and low carbon steel. The authors developed models and stated that, in terms of weld bead dimensions, the most influential parameter was welding speed. Reisgen et al. [25] optimized the parameters of the laser welded DP and TRIP steels to obtain the highest mechanical strength and minimum operation costs. Zhao et al. [26] investigated the effects of prescribed gap and laser welding parameters on the weld bead profile of galvanized steel sheets in a lap joint format and developed regression models. Benyounis et al. [27] reported the multi-response optimization of laser welded austenitic stainless steel. They developed mathematical models and established relationships between process parameters and responses, such as cost, tensile and impact strength.

As a result of the literature review, laser power, welding speed and focal position were found to be the most important welding parameters for welded joints' quality and mechanical performance. Due to the mechanical properties, especially tensile strength, being dependent on the weld bead geometry, heat input comes to the fore [19]. Although various studies examined the influence of laser parameters on the weld quality of dissimilar HSLA and DP steel joints, the information on fiber laser welding of dissimilar HSLA and MART steel sheets is still not quite clear. Whereas, resolving the issue of reducing vehicle mass while improving crash safety, the use of AHSS and HSLA is increasing. It is essential to investigate the effect of laser welding process parameters on the mechanical performance and quality of these steel types. Therefore, the aim of this work was to evaluate the effects of laser welding parameters of laser power, welding speed and focal position on the response, which was a proportional combination of tensile load (TL) and heat input (HI) using the Taguchi method. In this way, we will be able to find the optimal welding parameters that would maximize TL, while minimizing the HI of the fiber laser welded dissimilar HSLA and MART steel joints. In addition, for the selected samples, the microstructural and microhardness examinations were discussed.

2. Experimental Details

In this study, all experiments were carried out on 1.5 mm-thick cold rolled MART and HSLA steel sheets. The mechanical and chemical properties of the materials are shown in Table 1 [28]. The steel sheets were sheared into 250 mm × 80 mm coupons, which had the sheared edges placed together for running welds in butt joint configuration to make 250 mm × 160 mm, as shown in Figure 1a.

Table 1. Mechanical properties and chemical composition of the steels.

Material	C	Si	Mn	P	S	Al	Nb + Ti	Yield Strength (MPa)	Ultimate Strength (MPa)	Elongation (min %)
Docol 1200M	0.14	0.4	2.0	0.02	0.01	0.015	0.1	950	1200–1400	3
HSLA *	0.1	0.5	1.8	0.025	0.025	0.015	0.15	500	570–710	14

* HSLA: high strength low alloy.

The IPG ytterbium fiber laser attached to a Kuka robotic arm was used for welding experiments. The maximum power of the laser was 3 kW, and the wavelength was 1070 nm. The laser transmitted through the fiber optic cables and then came to a welding head. The fiber laser had a fiber core diameter of 0.2 mm with a laser beam spot diameter of 0.6 mm. The focal length was 300 mm. During the fiber laser welding process, no shielding gas was used.
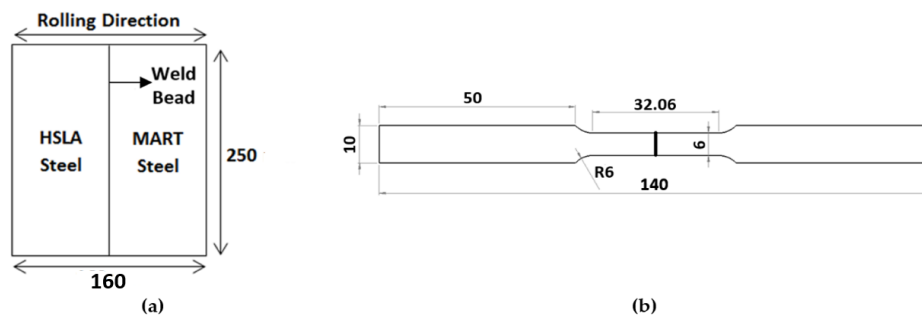
Figure 1. (**a**) Schematic illustration of the fiber laser welded steel sheets; (**b**) dimensions of the tensile test specimens. MART, martensitic steel.

In this study, for optimizing the process parameters, the Taguchi method was used. The parameter design is the key step in this method to achieving high quality without increasing cost. Firstly, a suitable orthogonal array should be selected depending on the total degree of freedom (DOF), which can be calculated by summing the individual DOF of each process parameter. The DOF for each parameter is the number of parameter levels minus 1. Then, the experiments were run based on the orthogonal array, analyzing the data and identifying the optimum parameters and, finally, if necessary, conducting confirmation trials with the optimal levels of the parameters. In this study, experiments were designed using an L25 orthogonal array, which means 25 rows and three columns. Five levels were considered for each of the three process parameters, which were laser power, welding speed and focal position. The levels of the parameters were chosen based on previous works in the literature and considering the laser system capabilities. Furthermore, trial experiments were applied to determine the operating range of each process parameter in order to produce an acceptable quality welding. The levels of the process parameters are shown in Table 2. A negative defocus is obtained when the focal point position is below the specimen surface.

Table 2. Laser welding process parameters and levels.

Variables	Unit	Symbol	Level 1	Level 2	Level 3	Level 4	Level 5
Laser Power	W	P	1000	1250	1500	1750	2000
Welding Speed	mm/s	S	5	15	25	35	45
Focal Position	mm	F	0	−0.2	−0.4	−0.6	−0.8

In the data analysis, in order to evaluate the effect of the selected parameters on the response, the signal-to-noise (S/N) ratios are calculated. In addition, S/N ratios are used to reduce the response variability. In this work, the larger-the-better S/N ratio was chosen in order to maximize the responses. The S/N ratio for the larger-the-better for the responses was calculated as follows:

$$S/N = -10\log\left(\frac{1}{n}\sum_{i=1}^{n}\frac{1}{y_i^2}\right) \tag{1}$$

where y_i is the response data from the experiment for the i-th parameter and n is the number of experiments. A higher S/N ratio indicates superior consideration for the optimal parameter combination, since the major signal dominates the noise. Equation (2) is used to calculate the parameter effects:

$$S/N_{i,j} = \frac{1}{n}\sum_{k=1}^{n}S/N_k \tag{2}$$

where $S/N_{i,j}$ is the average S/N value of the j-th level of the i-th parameter and n is the number of the experiment, which includes the j-th level of the i-th parameter. Additionally, the S/N_k is the value of

the *k*-th experiment S/N. Finally, a statistical analysis of variance (ANOVA) was used to indicate the relative effect of each process parameter on the responses.

At the metallographic examination stage of the study, the samples were cut from the weld cross-section using an electrical discharge cutting machine, then mounted in Bakelite, ground and polished up to 0.25-μm diamond paste. Two different etching procedures were conducted to reveal the grain boundaries and weld zone microstructure. In the first stage of the etching, 3% Nital solution was used. Then, to reveal some microstructures, subsequently, tint etched using 10% $Na_2S_2O_5$ was performed. Then, samples were analyzed for microstructural changes and possible defects using an optic microscope (OM, Nikon DIC, Tokyo, Japan) with the Clemex image analysis system and the scanning electron microscope (SEM, Zeiss EVO 40 XVP, Oberkochen, Germany). Vickers microhardness measurements (DUROLINE-M microhardness tester, Metkon, Turkey) were performed with a 200-g load, and 10-s dwell time. Tensile samples were machined from the perpendicular to the welding direction in accordance with ASTM, E8/E8M (Figure 1b). Tensile tests were performed using a computerized tensile testing machine (UTEST-7014, Ankara, Turkey) using a constant crosshead speed of 5 mm/min.

3. Results and Discussion

3.1. Optimization of the Process Parameters via the Taguchi Method

In this study, a Taguchi orthogonal array, which can handle five levels of the parameters with three columns and 25 rows, was used. The parameter optimization procedure was done in order to get a welded joint that has the maximum TL by minimizing the HI. HI plays a crucial role in the quality of the joint and indirectly the operation cost. The weld joint quality can be defined as weld bead geometry, mechanical properties and distortions [25]. Weld bead geometry, which means the bead width and penetration depth, is an important physical characteristic of a weldment, especially for dissimilar laser welding processes [19]. The appropriate weld bead geometry depends on the HI rate [22]. A shallower and inadequate penetration depth is related to an insufficient HI rate. Thence, the TL of the welded joint will decrease. However, a higher HI gives a slower cooling rate, and so, in the HAZ, large grain sizes can have poor toughness and decrease in TL. Hence, HI and, consequently, weld bead geometry affect the tensile strength of the joints [16,18]. Therefore, in this study, TL and HI were evaluated together as a response variable. Due to the tensile strength being the most important quality indicator of the welded joint, the effect ratio of the TL was determined to be higher, 60%. In determining the effect ratio of the HI, operational cost and weld bead geometry were considered. Namely, this ratio should not be too low because of the insufficient penetration, and also, it should not be too high in terms of cost and decreased strength of the joint. Therefore, it was determined to be 40%. In determining these effect ratios, they have also benefited from operational experience.

The TL of the laser welded joints was experimentally determined using tensile tests. At least three different specimens' tensile test results' average were taken. Additionally, HI was calculated by the laser power divided by the welding speed. Due to the scale of the values of TL and HI being different, a normalization process was applied to these values. Equation (3) was used for the normalization of the TL values.

$$X_n = \frac{X_i}{X_{\max}} \tag{3}$$

where X_n is the normalized value, X_i is the value of the relevant row and $X_{\max}$ is the maximum value. Since the objective function was a combination of the TL and HI, it is necessary to express it in the same form. Therefore, before applying Equation (3), the reciprocals of the HI values were taken using Equation (4) to convert the values to the larger the better form.

$$X_p = \frac{1}{X_i} \tag{4}$$

where X_p is a pre-normalized value, which was used in Equation (1), and X_i is the HI value of the relevant row.

The experimental layout for the process parameters, average TL, standard deviations (SD), HI values and normalized values are shown in Table 3. The S/N ratios for the response were calculated. The response column represents the sum of 60% normalized TL and 40% normalized HI. The S/N ratios of the process parameters were calculated by using Equation (2), and the effect of each parameter level was determined. As can be seen in Table 4, welding speed was the most important parameter for the response. Laser power and focal position followed this parameter, respectively.

Table 3. Design matrix with experimental results. TL, tensile load; HI, heat input.

Exp. No.	Parameters			Outputs and Calculations					Response	S/N Ratio
	Power (W)	Speed (mm/s)	Focal (mm)	TL (kN)	SD	Normalized TL	HI (J/mm)	Normalized HI		
1	1000	5	0	5.92	0.04	0.995	200.000	0.111	0.642	−3.849
2	1000	15	−0.2	5.49	0.05	0.923	66.667	0.333	0.687	−3.260
3	1000	25	−0.4	4.61	0.22	0.775	40.000	0.556	0.687	−3.260
4	1000	35	−0.6	3.43	0.11	0.578	28.571	0.778	0.658	−3.635
5	1000	45	−0.8	3.18	0.20	0.534	22.222	1.000	0.720	−2.853
6	1250	5	−0.2	5.88	0.02	0.990	250.000	0.089	0.629	−4.026
7	1250	15	−0.4	5.82	0.06	0.978	83.333	0.267	0.694	−3.172
8	1250	25	−0.6	5.32	0.08	0.894	50.000	0.444	0.714	−2.926
9	1250	35	−0.8	4.44	0.08	0.746	35.714	0.622	0.697	−3.135
10	1250	45	0	3.71	0.14	0.625	27.778	0.800	0.695	−3.160
11	1500	5	−0.4	5.73	0.04	0.964	300.000	0.074	0.608	−4.321
12	1500	15	−0.6	5.93	0.05	0.997	100.000	0.222	0.687	−3.260
13	1500	25	−0.8	5.93	0.06	0.997	60.000	0.370	0.746	−2.545
14	1500	35	0	5.82	0.00	0.979	42.857	0.519	0.795	−1.992
15	1500	45	−0.2	4.30	0.10	0.723	33.333	0.667	0.701	−3.085
16	1750	5	−0.6	5.52	0.06	0.929	350.000	0.063	0.583	−4.686
17	1750	15	−0.8	5.90	0.02	0.992	116.667	0.190	0.671	−3.465
18	1750	25	0	5.79	0.10	0.974	70.000	0.317	0.712	−2.950
19	1750	35	−0.2	5.87	0.02	0.987	50.000	0.444	0.770	−2.270
20	1750	45	−0.4	5.95	0.01	1.000	38.889	0.571	0.829	−1.628
21	2000	5	−0.8	5.52	0.07	0.929	400.000	0.056	0.579	−4.746
22	2000	15	0	5.87	0.10	0.987	133.333	0.167	0.659	−3.622
23	2000	25	−0.2	5.58	0.08	0.938	80.000	0.278	0.674	−3.426
24	2000	35	−0.4	5.62	0.04	0.946	57.143	0.389	0.723	−2.817
25	2000	45	−0.6	5.67	0.05	0.953	44.444	0.500	0.772	−2.247

Table 4. Response table for the S/N ratios for the objective.

Level	Laser Power	Welding Speed	Focal Position
1	−3.372	−4.326	−3.349
2	−3.284	−3.356	−3.351
3	−3.041	−3.022	−3.040
4	−3.000	−2.770	−3.214
5	−3.372	−2.595	−3.115
Delta	0.372	1.731	0.311
Rank	2	1	3

The S/N ratios' main effect plot showed how each process parameter affects the response characteristic. The means of the S/N ratios exhibit a good correlation with the main effects of the mean of means (Figure 2). This result indicates that process parameters show higher mean values resulting in higher variability. The response seems to be mainly affected by the process parameters, as shown in Figure 2. It can be seen that the welding speed was the most important process parameter that affected

the response. There was a small difference between laser power and focal position; while the focal position plots showed the lowest effect on the response to those parameters.
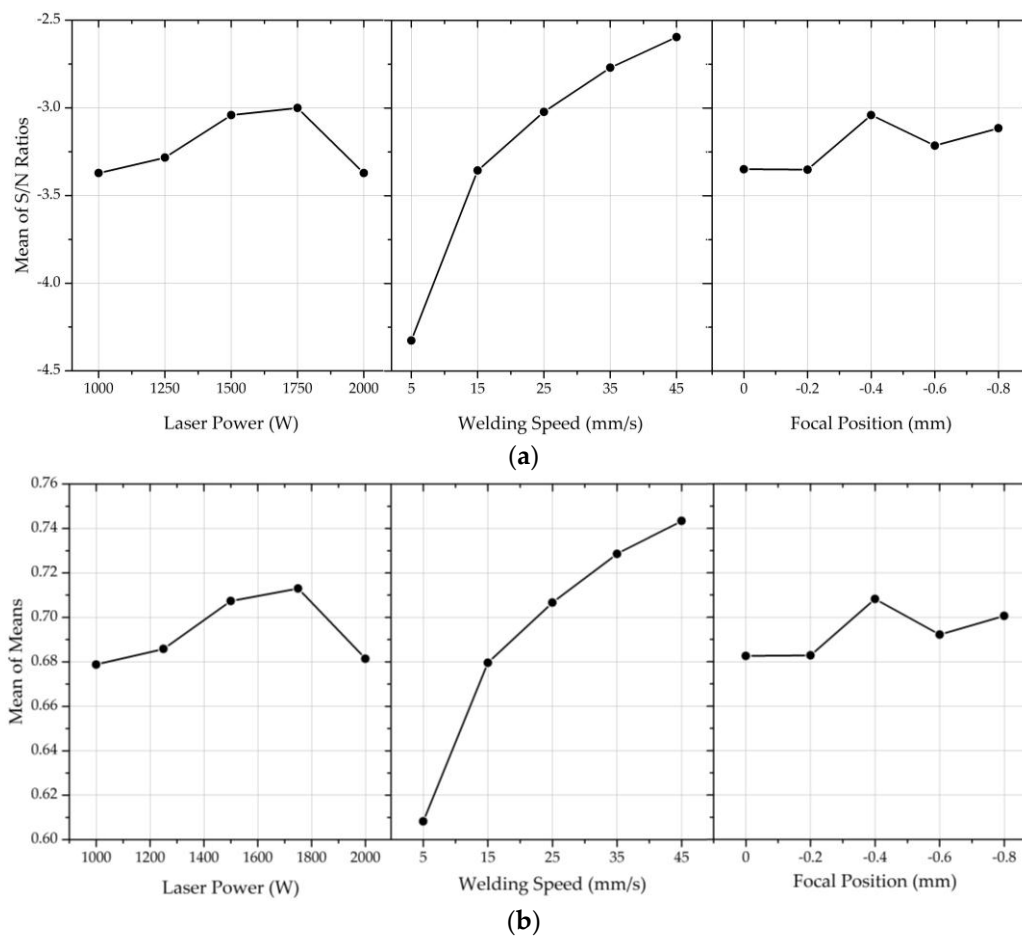

Figure 2. Effects plots of (**a**) S/N ratios; and (**b**) mean of means for the response.

In this study, the optimal parameter combination was found to be 1750 W for laser power, 45 mm/s for welding speed and −0.4 mm for the focal position. This parameter combination was Sample 20 in the orthogonal array in Table 3; thus, no additional confirmation experiments were required.

3.2. Analysis of Variance

The order of importance of the parameters on the response was determined using ANOVA. By comparing the estimation of the experimental errors against the mean square, ANOVA tests the importance of all main factors and their interactions. In this study, The ANOVA shows that for the response (maximum TL and minimum HI), welding speed has the greatest effect with a contribution of 64.01 percent. Laser power and focal position effects were 5.60% and 2.82%, respectively (Table 5). This result is compatible with Table 4, which is the response table for the S/N ratios. Due to the interactions between the processes parameters not being defined, the residual error was large in ANOVA.

Table 5. Analyses of variance table for means.

Source	Degrees of Freedom (DF)	Sum of Squares (Seq SS)	Adjusted Mean Squares (Adj MS)	F	p	Contribution (%)
Laser Power	4	0.004975	0.001244	0.61	0.663	5.60
Welding Speed	4	0.056813	0.014203	6.97	0.004	64.01
Focal Position	4	0.002506	0.000627	0.31	0.867	2.82
Residual Error	12	0.024450	0.002038			27.55
Total	24	0.088745				

3.3. Effects of Process Parameters on the Response

In this study, it was observed that welding speed was a significant parameter that affects the response, which is maximum TL and minimum HI. Although the effect of laser power may seem quite small in ANOVA results, it is an important process parameter due to the associated HI. The increase of laser power causes more heat input. Under the high laser power, if the welding speed were not chosen properly, the weld bead would be broadened and the surface quality of the weld decreased. Therefore, the laser power and welding speed should be considered together to get good weld profiles and TL. When the laser power was kept constant, with increasing welding speed, HI decreased. Due to weld bead geometry related to the HI, weld bead width was increased with increasing HI. In all laser power levels, when the speed was 5 mm/s, the beads were larger due to the excessive heat input (Figure 3a). On the other side, when the speed was 45 mm/s, the beads were found to be narrower (Figure 3b).
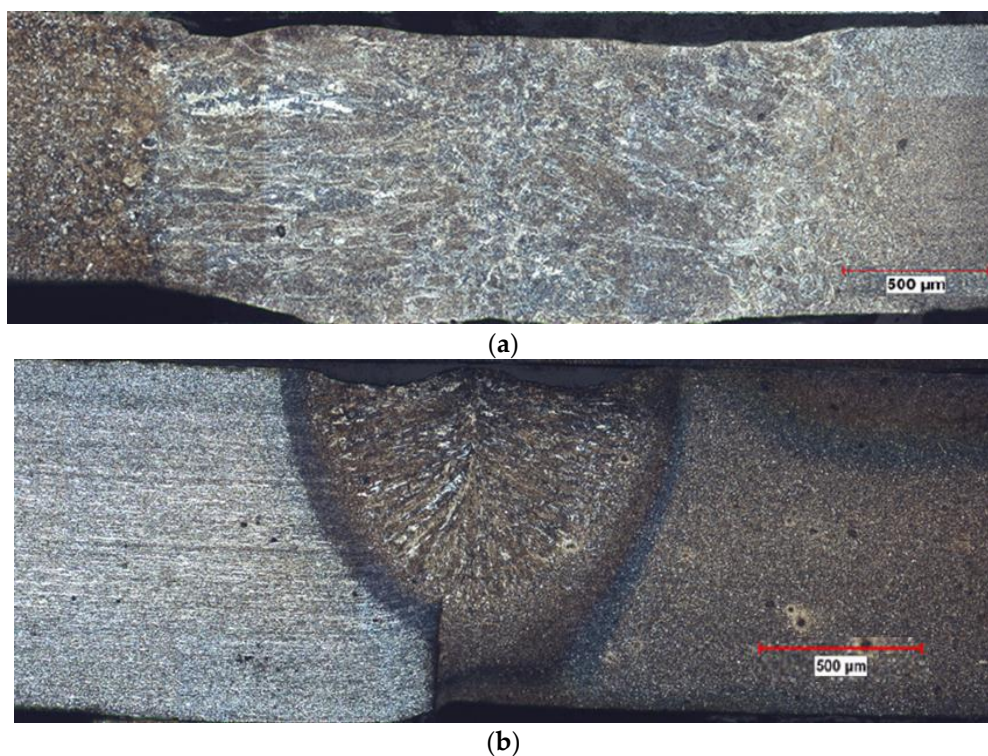

(**a**)

(**b**)

Figure 3. Transverse sections of the joints using different heat inputs: (**a**) 300 J/mm, Sample 11; (**b**) 44 J/mm, Sample 25.

As known weld bead dimensions directly affect the TL of the joints [25], at insufficient HI at the low laser power levels or high welding speeds, adequate penetration did not occur, and the TL of the joints was decreased. Besides, at excessive HI levels, the HAZ would be wider, and that causes a decrease in TL. According to the tensile test results, the welding speed in the range between 35 mm/s and 45 mm/s would lead to minimum HI and acceptable TL for the joints. The focal position

determines the laser spot size and consequently the power density on the surface, depending on the optical path. In this study, the focal position has the lowest effect on the response. It is believed that the level range of this parameter caused this situation due to the range of the spot diameters being quite small.

3.4. Microstructure and Microhardness Evolution

The microstructural examination and microhardness evolution of the selected welds that have the highest (Sample 20) and lowest (Sample 21) response values were discussed. Three different zones, including FZ, HAZ and base metal (BM), were revealed by examining the selected sample's cross-sections. The BM of the HSLA consisted of a ferrite matrix with carbides dispersed in the grains and at the grain boundaries (Figure 4a). As shown in Figure 4b, MART steels were comprised of martensitic microstructures and a small proportion of ferritic and bainitic grains.
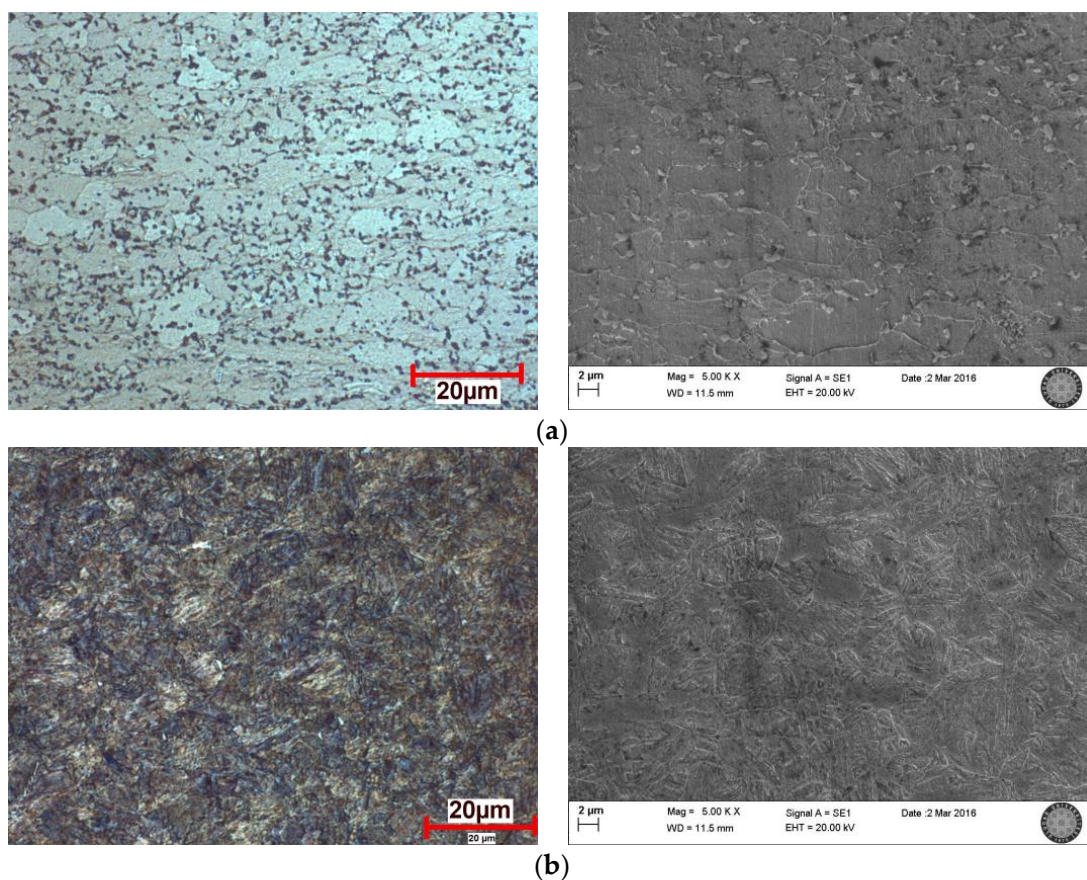
Figure 4. Optical micrograph and SEM views of the: (**a**) HSLA base metal (BM); (**b**) MART BM.

In the welding process, final microstructures are affected by peak temperature and the cooling rate of the relevant zones, and carbon equivalent (CE) value resulted from the chemistry of the steels [29–32]. Although there are numerous formulae for calculating CE, Yurioka's formula was used in this study because of its suitability for C-Mn steels [33]. The CE values of steels were calculated using Yurioka's formula given by Equation (5) and shown in Table 6 [34,35]. The Ti element was considered as the Nb element because of their similar effect on the steels' hardenability.

$$CE = C + f(C) \left[\frac{Si}{24} + \frac{Mn}{6} + \frac{Cu}{15} + \frac{Ni}{20} + \frac{(Cr + Mo + Nb + V)}{5} \right] \tag{5}$$

where $f(C)$ is the accommodation factor and is calculated as;

$$f(C) = 0.75 + 0.25\tanh\left[20\left(C - 0.12\right)\right] \tag{6}$$

Table 6. The carbon equivalent (CE) values of the HSLA and MART steels. FZ, fusion zone.

Calculated Zone	HSLA	MART	FZ
CE	0.330	0.453	0.391

The microstructure of the FZ of Sample 20, with a 0.391 CE value (average of MART and HSLA steels), is predominantly martensite with a bainitic structure (Figure 5). With the effect of the heat exchange gradient, in the vicinity of the fusion boundary, grains were elongated towards the weld center. However, in the center of the FZ, equiaxed grains were observed (Figure 5a). Furthermore, due to the lack of shielding gas, as a possible result of the diffusion of some elements, i.e., oxygen and nitrogen from the air, it is thought to be some inclusions in the FZ, which were marked with yellow arrows in Figure 5b.

(**a**)　　　　　　　　　　　　　　　　(**b**)
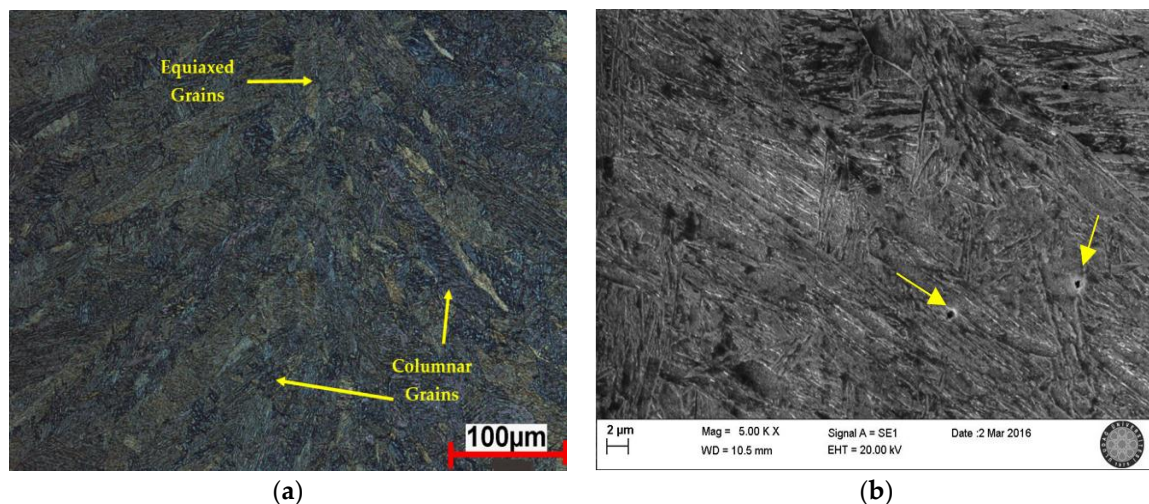
Figure 5. (**a**) Optical micrograph; and (**b**) SEM micrograph showing the FZ of the Sample 20.

Weld zone microstructures of Sample 21, which have the highest heat input and, of course, slowest cooling rate, are completely different from Sample 20 and not associated with the CE values due to the slow cooling conditions. The FZ of Sample 21 consisted of ferritic microstructures with multiple morphologies, e.g., grain boundary, acicular and Widmanstatten (Figure 6a). Due to the oriented solidification and slow cooling rate, elongated and extremely coarse grains were revealed. In Figure 6b, grain boundaries were dashed with yellow, which contain different ferritic structures. Acicular ferritic microstructures can also be seen in Figure 6. The yellow arrows show the inclusions where acicular ferrites nucleated (Figure 6c).
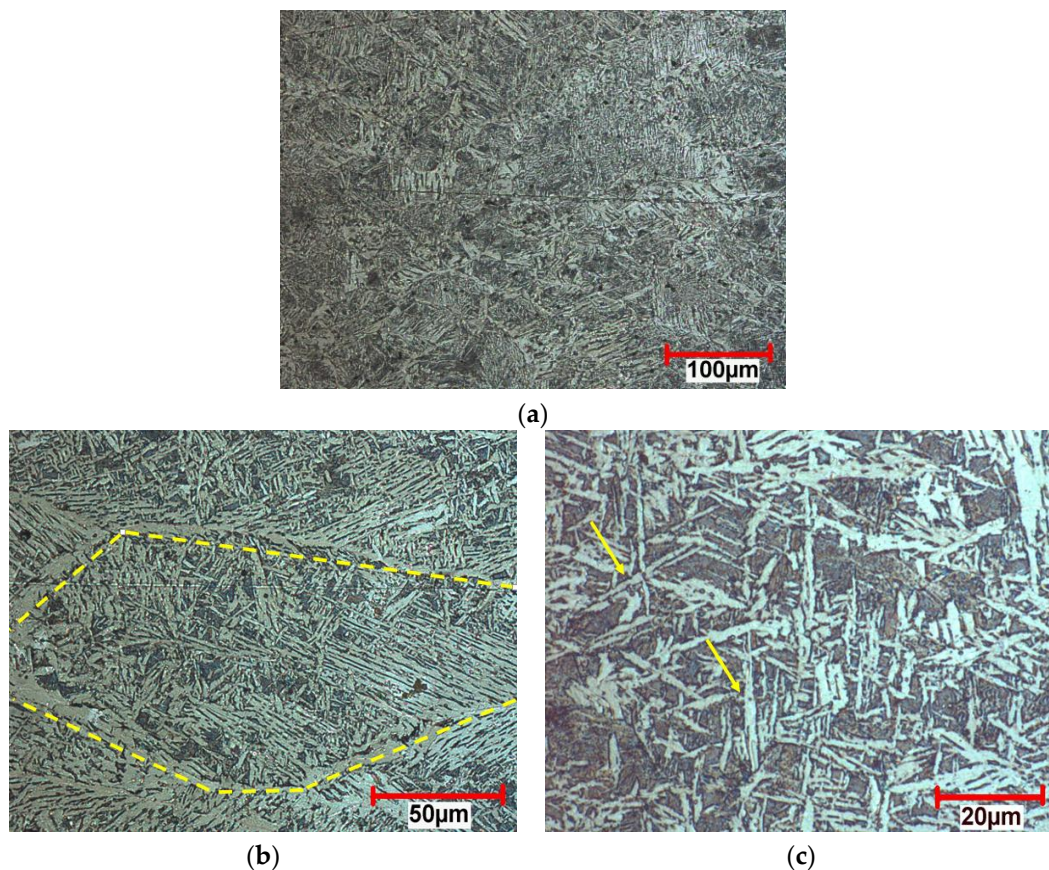
Figure 6. Detailed different magnifications of FZ microstructures of Sample 21: (**a**) FZ at ×100 magnification; (**b**) extremely coarse grains in FZ; and (**c**) inclusions in FZ.

The HAZ of Sample 20 can be divided into five subzones, namely partially molten zone (PMZ), coarse-grained HAZ (CGHAZ), fine-grained (FGHAZ), inter-critical HAZ (ICHAZ) and sub-critical HAZ (SCHAZ). Optical micrographs of these different subzones can be seen in Figures 7 and 8. In the microstructural examinations, PMZ could not be observed. Both MART and HSLA steel, in CGHAZ, consisted of martensitic-bainitic microstructure as a result of the transformation of coarsened austenite grains (Figures 7a and 8a). While the CGHAZ of MART steel shows a higher proportion of martensitic and lower proportion of bainitic microstructures, HSLA steel shows a higher proportion of bainitic and lower proportion of martensitic microstructures. This can be attributed to the CE values of the steels. A higher CE value promoted the formation of martensite, whereas a lower CE value promoted bainitic structures. Although the FGHAZ of MART steel's microstructure is similar to CGHAZ, but consisted of finer grains, this zone could not be observed in HSLA steel. In the ICHAZ, where the peak temperature is between A_3 and A_1, the partial transformation of ferrite to a mixture of ferrite and austenite resulted in martensite islands between the fine-grained ferrite matrix and carbides in HSLA steel (Figure 7b) [2]. Figure 7b shows a transition zone towards SCHAZ.
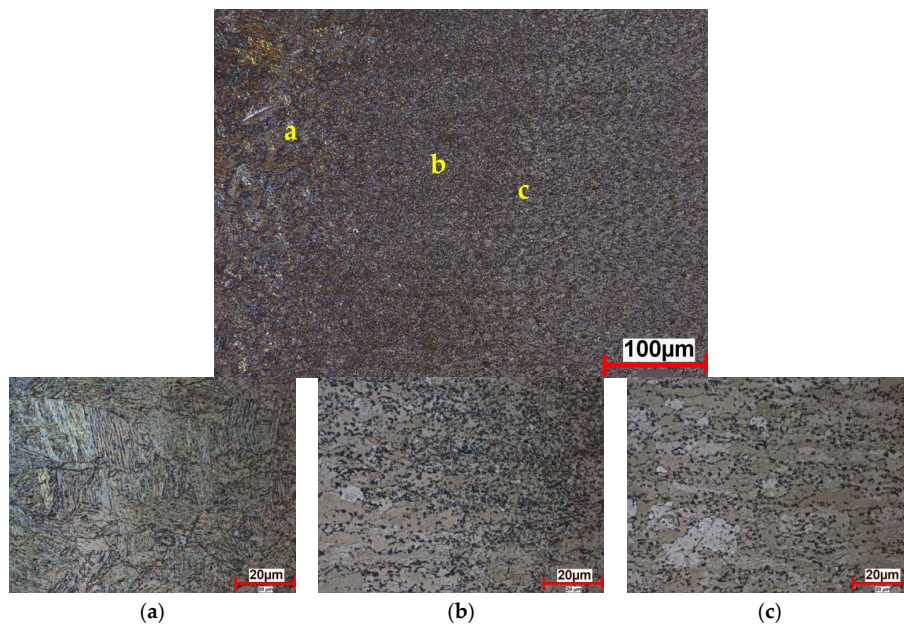
(**a**)   (**b**)   (**c**)

Figure 7. Detailed heat affected zone (HAZ) microstructures and subzones of the HSLA side of Sample 20: (**a**) coarse-grained HAZ (CGHAZ); (**b**) inter-critical HAZ (ICHAZ); and (**c**) sub-critical HAZ (SCHAZ).
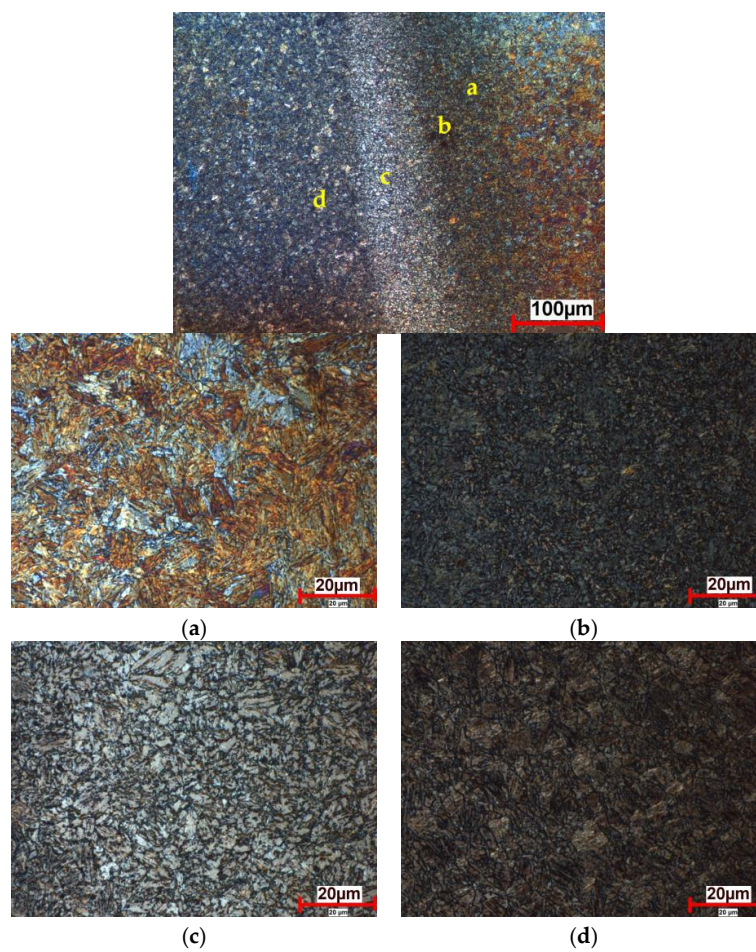

(**a**)   (**b**)

(**c**)   (**d**)

Figure 8. Detailed HAZ microstructures and subzones of the MART side of Sample 20: (**a**) CGHAZ; (**b**) fine-grained (FGHAZ); (**c**) ICHAZ; and (**d**) SCHAZ.

The ICHAZ of MART steel exhibited a dual phase microstructure containing ferrite with fine and well-dispersed martensite. In addition, some portion of the acicular ferritic microstructures can be seen in Figure 8c. Since shielding gas was not used, nitrogen and oxygen absorption could promote titanium base nitrides, carbo-nitrides and oxide inclusions where acicular ferrites can nucleate [2,36–38]. Furthermore, the slow cooling rate of this zone could induce ferritic structures to be formed. Figure 8d shows the SCHAZ of MART steel. In this zone, tempered martensite and bainite formed due to the lower peak temperature than A_1. However, it is expected that the coarsening of the carbides occurs in the HSLA side, and there is no difference identified metallographically. This can be related to the thermal stability of the HSLA, which is greater than MART and, therefore, does not have a microstructure that is distinct from its BM [2].

For Sample 21, the whole weld zone was roughly 11 mm, so only the micrographs of specific zones are presented here. The CGHAZ of HSLA side of Sample 21 consisted of ferritic and bainitic structures and it is shown with dashed lines. The FGHAZ of the HSLA side contains similar, but finer grains with respect to CGHAZ (Figure 9b). Beside the FGHAZ, coarsening of the carbides occurred in the HSLA side.
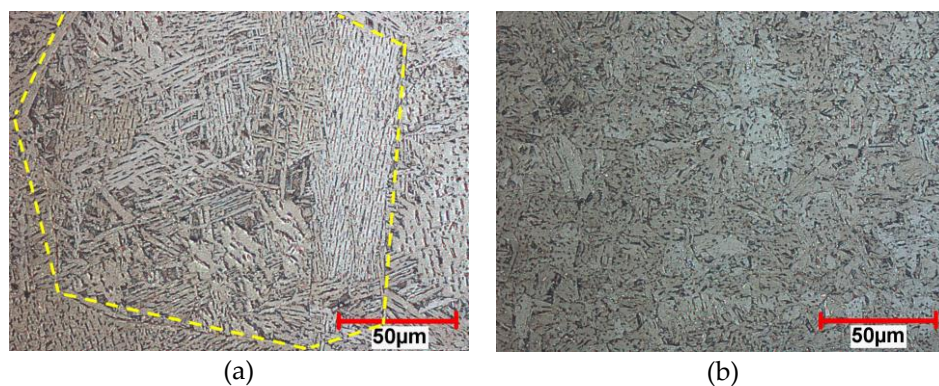

(a)   (b)

Figure 9. Microstructures of the HAZ zone for HSLA side of Sample 21: (**a**) CGHAZ and (**b**) FGHAZ.

In the CGHAZ and FGHAZ of the MART side of Sample 21, as a result of the higher CE, coarse baiting, ferritic and martensitic microstructures were identified (Figure 10a,b). The ICHAZ, in accordance with the Fe-Fe$_3$C equilibrium diagram, consisted of fine ferritic structures with small portions of pearlitic structures (Figure 10c). As expected, under the influence of a relatively high temperature, which is in the range of martensite tempering temperatures, tempered martensite formed in SCHAZ of the MART side (Figure 10d).

Microhardness measurements were conducted in the various zones of Samples 20 and 21. The microhardness of the BM of the HSLA and MART steels was measured as 213 and 404 Vickers, respectively. The hardness profile of the welded joint section varies significantly because of the phase transformations during the thermal cycle of the welding process. Figure 11 shows the microhardness map of Sample 20. Figure 11 also presents the microhardness profile across the mid-section of the sample. Due to the rapid cooling of FZ, each material showed an increase in hardness of FZ relative to BM. The average microhardness value in the FZ is 480 Vickers and varies across the section. This fluctuation is attributed to the mixed microstructure of the FZ. Different hardness of the martensitic and bainitic microstructures could cause the fluctuation of the hardness profile. In addition, various morphologies (i.e., columnar and equiaxed) in FZ could be a reason for the various hardness. However, some researchers have focused to determine an empirical formula for FZ hardness using CE values; in the present study, the measured hardness of FZ is higher than the calculated values using the mentioned formulas [31,36]. The calculated hardness values using the formulas given in the literature are 434 HV and 365 HV. In all compared zones, MART steel exhibited higher hardness values due to the higher CE value, which has a significant influence on the hardenability. While the hardness of the

HSLA side exhibits a sharp increase through the HAZ up to the FZ, the MART side shows a softening zone in HAZ. The continuous increase trend in the HSLA side was due to the ferritic microstructure of HSLA steel. The tempering zone and ferritic/martensitic dual phase structures in MART steel caused a decrease in hardness.
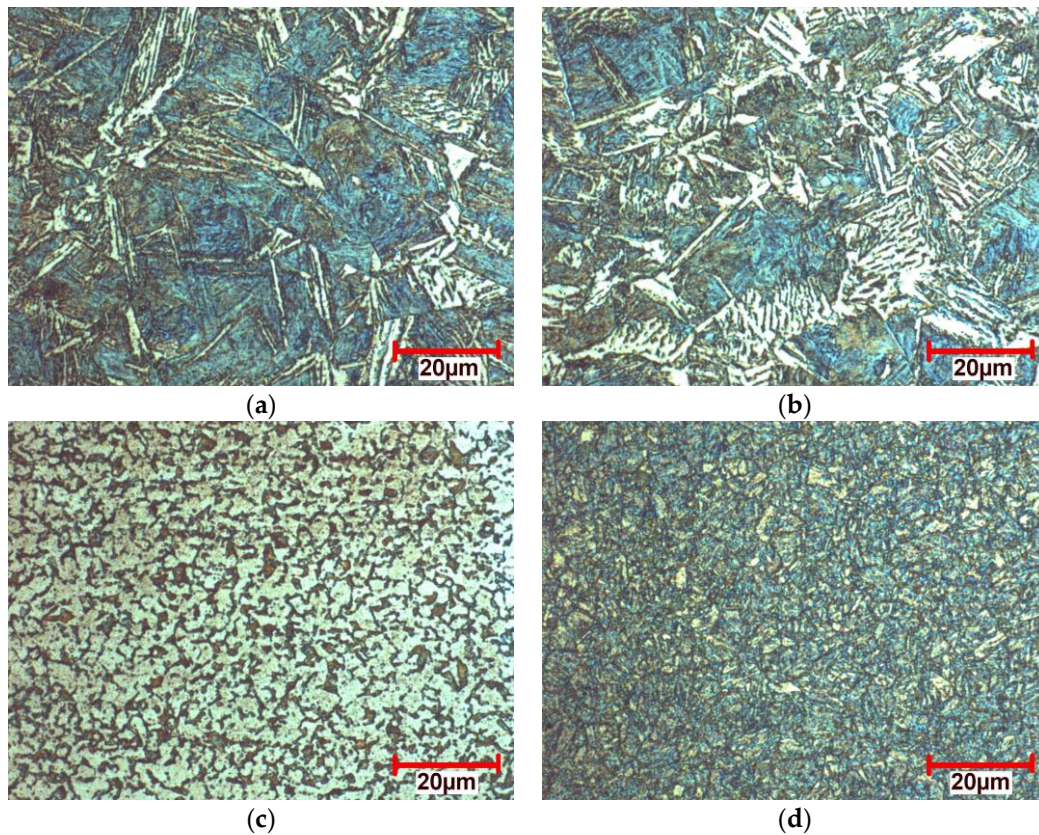

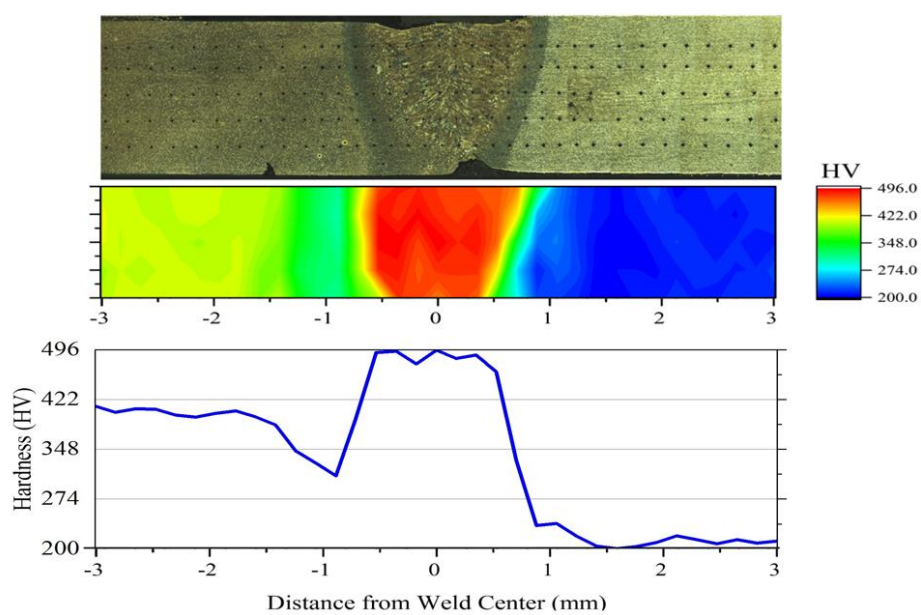**Figure 10.** Detailed HAZ microstructures and subzones of the MART side of Sample 21: (**a**) CGHAZ; (**b**) FGHAZ; (**c**) ICHAZ; and (**d**) SCHAZ.

Figure 11. Microhardness map and profile of Sample 20.

The microhardness map and profile of Sample 21 can be seen in Figure 12. The highest and the lowest microhardness values were measured in the BM of MART and HSLA, respectively. The highest value is related to the predominantly martensitic microstructure of the BM of MART steel. Among the weld zone of the MART steel, the ICHAZ showed the lowest microhardness corresponding with the ferritic-pearlitic microstructure. The measured microhardness values through the FZ showed a fluctuation, which can be a result of multiple morphologies of ferritic structures. In the HSLA side, microhardness values showed a decreasing trend up to the BM.
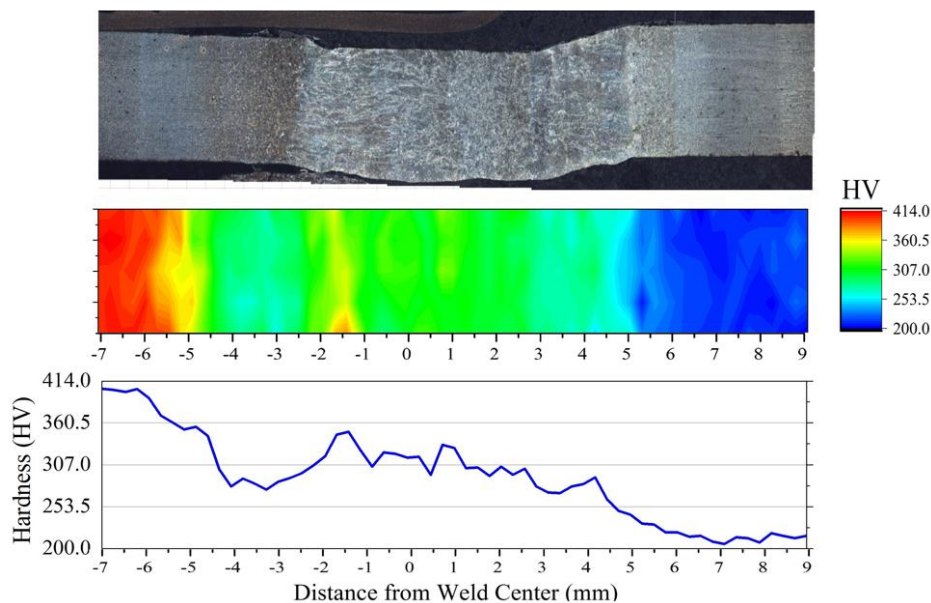

Figure 12. Microhardness map and profile of Sample 21.

4. Conclusions

In this study, fiber laser welded dissimilar MART and HSLA steels have been evaluated with respect to tensile properties, microstructure and hardness profile. As the first step of this study, the process parameters of laser welded dissimilar steel joints have been optimized to maximize the TL and minimize the HI of the welded joints using the Taguchi method. The order of importance of the process parameters on the response was welding speed, laser power and focal position. The welding speed was found to be the most effective process parameter, and its interaction with the laser power should be monitored for the HI and TL of the joints. It was observed that, if the HI was not sufficient due to high speed or low laser power, the weld bead geometry was not formed appropriately. In addition, when applying excessive HI, the HAZ would be wider, and that causes a decrease in TL. The optimum combination of laser welding process parameters was a welding speed of 45 mm/s, a laser power of 1750 W and the focal position of −0.4 mm.

In the second step, the microstructural examination and microhardness evolution of the selected welds that have the highest and lowest response values were discussed. Weld zone microstructures of selected samples were completely distinct due to the different HI and consequently not associated with CE values due to slow cooling rates. The HAZ of the samples was divided into five subzones, namely PMZ, CGHAZ, FGHAZ, ICHAZ and SCHAZ, due to the grain transformations. Due to the phase transformations during the thermal cycle of the process, the hardness profile of the welded sections varies significantly. Due to the rapid cooling of FZ, each sample showed an increase in hardness of FZ relative to BM. While the hardness of the HSLA side exhibits a sharp increase through the HAZ up to the FZ, the MART side shows a softening zone in HAZ.

Author Contributions: Celalettin Yuce and Fatih Karpat conceived of and designed the experiments. Celalettin Yuce and Mumin Tutar performed the experiments and microstructural examination. Celalettin Yuce, Mumin Tutar and Nurettin Yavuz analyzed the data. All of the authors discussed the results and commented on the manuscript at all stages. All co-authors contributed to the manuscript proofing and submissions.

Conflicts of Interest: The authors declare no conflict of interest.

References

1. Kuziak, R.; Kawalla, R.; Waengler, S. Advanced high strength steels for automotive industry. *Arch. Civ. Mech. Eng.* **2008**, *8*, 103–117. [CrossRef]

2. Saha, D.C.; Westerbaan, D.; Nayak, S.S.; Biro, E.; Gerlich, A.P.; Zhou, Y. Microstructure-properties correlation in fiber laser welding of dual-phase and HSLA steels. *Mater. Sci. Eng. A* **2014**, *607*, 445–453. [CrossRef]

3. Liu, Y.; Dong, D.; Wang, L.; Chu, X.; Wang, P.; Jin, M. Strain rate dependent deformation and failure behavior of laser welded DP780 steel joint under dynamic tensile loading. *Mater. Sci. Eng. A* **2015**, *627*, 296–305. [CrossRef]

4. Benasciutti, D.; Lanzutti, A.; Rupil, G.; Haeberle, E.F. Microstructural and mechanical characterisation of laser-welded lap joints with linear and circular beads in thin low carbon steel sheets. *Mater. Des.* **2014**, *62*, 205–216. [CrossRef]

5. Casalino, G.; Dal Maso, U.; Angelastro, A.; Campanelli, S.L. Hybrid laser welding: A review. *DAAAM Int. Sci. Book* **2010**, *38*, 413–430.

6. Xu, W.; Westerbaan, D.; Nayak, S.S.; Chen, D.L.; Goodwin, F.; Zhou, Y. Tensile and fatigue properties of fiber laser welded high strength low alloy and DP980 dual-phase steel joints. *Mater. Des.* **2013**, *43*, 373–383. [CrossRef]

7. Parkes, D.; Xu, W.; Westerbaan, D.; Nayak, S.S.; Zhou, Y.; Goodwin, F.; Bhole, S.; Chen, D.L. Microstructure and fatigue properties of fiber laser welded dissimilar joints between high strength low alloy and dual-phase steels. *Mater. Des.* **2013**, *51*, 665–675. [CrossRef]

8. Parkes, D.; Westerbaan, D.; Nayak, S.S.; Zhou, Y.; Goodwin, F.; Bhole, S.; Chen, D.L. Tensile properties of fiber laser welded joints of high strength low alloy and dual-phase steels at warm and low temperatures. *Mater. Des.* **2014**, *56*, 193–199. [CrossRef]

9. Wang, J.; Yang, L.; Sun, M.; Liu, T.; Li, H. Effect of energy input on the microstructure and properties of butt joints in DP1000 steel laser welding. *Mater. Des.* **2016**, *90*, 642–649. [CrossRef]

10. Wang, J.; Yang, L.; Sun, M.; Liu, T.; Li, H. A study of the softening mechanisms of laser-welded DP1000 steel butt joints. *Mater. Des.* **2016**, *97*, 118–125. [CrossRef]

11. Rossini, M.; Spena, P.R.; Cortese, L.; Matteis, P.; Firrao, D. Investigation on dissimilar laser welding of advanced high strength steel sheets for the automotive industry. *Mater. Sci. Eng. A* **2015**, *628*, 288–296. [CrossRef]

12. Němeček, S.; Mužík, T.; Míšek, M. Differences between laser and arc welding of HSS steels. *Phys. Proced.* **2012**, *39*, 67–74. [CrossRef]

13. Zhao, Y.Y.; Zhang, Y.S.; Hu, W. Effect of welding speed on microstructure, hardness and tensile properties in laser welding of advanced high strength steel. *Sci. Technol. Weld. Join.* **2013**, *18*, 581–590. [CrossRef]

14. Arslanoglu, N.; Yigit, A. Experimental investigation of radiation effect on human thermal comfort by Taguchi method. *Appl. Therm. Eng.* **2016**, *92*, 18–23. [CrossRef]

15. Tutar, M.; Aydin, H.; Yuce, C.; Yavuz, N.; Bayram, A. The optimisation of process parameters for friction stir spot-welded AA3003-H12 aluminium alloy using a Taguchi orthogonal array. *Mater. Des.* **2014**, *63*, 789–797. [CrossRef]

16. Benyounis, K.Y.; Olabi, A.G. Optimization of different welding processes using statistical and numerical approaches—A reference guide. *Adv. Eng. Softw.* **2008**, *39*, 483–496. [CrossRef]

17. Anawa, E.M.; Olabi, A.G. Optimization of tensile strength of ferritic/austenitic laser-welded components. *Opt. Lasers Eng.* **2008**, *46*, 571–577. [CrossRef]

18. Anawa, E.M.; Olabi, A.G. Using Taguchi method to optimize welding pool of dissimilar laser-welded components. *Opt. Laser Technol.* **2008**, *40*, 379–388. [CrossRef]

19. Sathiya, P.; Jaleel, M.Y.A.; Katherasan, D.; Shanmugarajan, B. Optimization of laser butt welding parameters with multiple performance characteristics. *Opt. Laser Technol.* **2011**, *43*, 660–673. [CrossRef]

20. Casalino, G.; Campanelli, S.L.; Ludovico, A.D. Laser-arc hybrid welding of wrought to selective laser molten stainless steel. *Int. J. Adv. Manuf. Technol.* **2013**, *68*, 209–216. [CrossRef]

21. Acherjee, B.; Kuar, A.S.; Mitra, S.; Misra, D. A sequentially integrated multi-criteria optimization approach applied to laser transmission weld quality enhancement—A case study. *Int. J. Adv. Manuf. Technol.* **2013**, *65*, 641–650. [CrossRef]

22. Benyounis, K.Y.; Olabi, A.G.; Hashmi, M.S.J. Effect of laser welding parameters on the heat input and weld-bead profile. *J. Mater. Process. Technol.* **2005**, *164*, 978–985. [CrossRef]

23. Ruggiero, A.; Tricarico, L.; Olabi, A.G.; Benyounis, K.Y. Weld-bead profile and costs optimisation of the CO_2 dissimilar laser welding process of low carbon steel and austenitic steel AISI316. *Opt. Laser Technol.* **2011**, *43*, 82–90. [CrossRef]

24. Olabi, A.G.; Alsinani, F.O.; Alabdulkarim, A.A.; Ruggiero, A.; Tricarico, L.; Benyounis, K.Y. Optimizing the CO_2 laser welding process for dissimilar materials. *Opt. Lasers Eng.* **2013**, *51*, 832–839. [CrossRef]

25. Reisgen, U.; Schleser, M.; Mokrov, O.; Ahmed, E. Optimization of laser welding of DP/TRIP steel sheets using statistical approach. *Opt. Laser Technol.* **2012**, *44*, 255–262. [CrossRef]

26. Zhao, Y.; Zhang, Y.; Hu, W.; Lai, X. Optimization of laser welding thin-gage galvanized steel via response surface methodology. *Opt. Lasers Eng.* **2012**, *50*, 1267–1273. [CrossRef]

27. Benyounis, K.Y.; Olabi, A.G.; Hashmi, M.S.J. Multi-response optimization of CO_2 laser-welding process of austenitic stainless steel. *Opt. Laser Technol.* **2008**, *40*, 76–87. [CrossRef]

28. SSAB Products. Available online: http://www.ssab.com/products/brands/docol (accessed on 22 August 2016).

29. Guo, W.; Crowther, D.; Francis, J.A.; Thompson, A.; Liu, Z.; Li, L. Microstructure and mechanical properties of laser welded S960 high strength steel. *Mater. Des.* **2015**, *85*, 534–548. [CrossRef]

30. Khan, M.I.; Kuntz, M.L.; Biro, E.; Zhou, Y. Microstructure and mechanical properties of resistance spot welded advanced high strength steels. *Mater. Trans.* **2008**, *49*, 1629–1637. [CrossRef]

31. Oyyaravelu, R.; Kuppan, P.; Arivazhagan, N. Metallurgical and Mechanical properties of Laser welded High Strength Low Alloy Steel. *J. Adv. Res.* **2016**, *7*, 463–472. [CrossRef] [PubMed]

32. Coelho, R.S.; Corpas, M.; Moreto, J.A.; Jahn, A.; Standfuß, J.; Kaysser-Pyzalla, A.; Pinto, H. Induction-assisted laser beam welding of a thermomechanically rolled HSLA S500MC steel: A microstructure and residual stress assessment. *Mater. Sci. Eng. A* **2013**, *578*, 125–133. [CrossRef]

33. Talaş, Ş. The assessment of carbon equivalent formulas in predicting the properties of steel weld metals. *Mater. Des.* **2010**, *31*, 2649–2653. [CrossRef]

34. Yurioka, N. Carbon Equivalents for Hardenability and Cold Cracking Susceptibility of Steels. In Proceedings of the Select Conference on Hardenability of Steels, Derby, UK, 17 May 1990.

35. Santillan Esquivel, A.; Nayak, S.S.; Xia, M.S.; Zhou, Y. Microstructure, hardness and tensile properties of fusion zone in laser welding of advanced high strength steels. *Can. Metall. Q.* **2012**, *51*, 328–335. [CrossRef]

36. Midawi, A.R.H.; Santos, E.B.F.; Huda, N.; Sinha, A.K.; Lazor, R.; Gerlich, A.P. Microstructures and mechanical properties in two X80 weld metals produced using similar heat input. *J. Mater. Process. Technol.* **2015**, *226*, 272–279. [CrossRef]

37. Beidokhti, B.; Kokabi, A.H.; Dolati, A. A comprehensive study on the microstructure of high strength low alloy pipeline welds. *J. Alloys Compd.* **2014**, *597*, 142–147. [CrossRef]

38. Beidokhti, B.; Dolati, A.; Koukabi, A.H. Effects of alloying elements and microstructure on the susceptibility of the welded HSLA steel to hydrogen-induced cracking and sulfide stress cracking. *Mater. Sci. Eng. A* **2009**, *507*, 167–173. [CrossRef]